Journal of Advanced Ceramics
2022, **11**(10): 1559–1570
https://doi.org/10.1007/s40145-022-0629-8
ISSN 2226-4108
CN 10-1154/TQ

Research Article

Oxygen vacancy engineering on cerium oxide nanowires for room-temperature linalool detection in rice aging

Jinyong XU, Chao ZHANG*

College of Mechanical Engineering, *Yangzhou University*, *Yangzhou 225127*, *China*

Received: April 21, 2022; Revised: June 18, 2022; Accepted: July 2, 2022

Abstract: It is a huge challenge for metal oxide semiconductor gas sensors to inspect volatile organic compounds (VOCs) at room temperature (RT). Herein, the effective utilization of cerium oxide (CeO_2) nanowires for RT detection of VOCs was realized via regulating its surface chemical state. Oxygen vacancy engineering on CeO_2 nanowires, synthesized via hydrothermal method, can be manipulated by annealing under various controlled atmospheres. The sample annealed under 5%H_2+95%Ar condition exhibited outstanding RT sensing properties, displaying a high response of 16.7 towards 20 ppm linalool, a fast response and recovery time (16 and 121 s, respectively), and a low detection of limit of 0.54 ppm. The enhanced sensing performance could be ascribed for the synergistic effects of its nanowire morphology, the large specific surface area (83.95 m^2/g), and the formation of extensive oxygen vacancy accompanied by an increase in Ce^{3+}. Additionally, the practicability of the sensor was verified via two varieties of rice (Indica and Japonica rice) stored in various periods (1, 3, 5, 7, 15, and 30 d). The experimental results revealed that the sensor was able to distinguish Indica rice from Japonica rice. Accordingly, the as-developed sensor delivers a strategic material to develop high-performance RT electronic nose equipment for monitoring rice quality.

Keywords: cerium oxide (CeO_2); nanowire; oxygen vacancy; linalool; gas sensor

1 Introduction

Linalool, one of the alcohols generated via the further breakdown of aldehydes, played a major contribution to the rice profile in the process of aging [1]. And its content change could be considered to be an index for the inspection of rice quality. Accordingly, monitoring and identifying the linalool concentration is an effective method for the evaluation of rice quality. Currently, various traditional methods (e.g., liquid chromatography–mass spectrometry [2], near-infrared spectroscopy [3], and gas chromatography–mass spectrometry [4]) have been available for determining the linalool content in rice aging. Except for outstanding stability and high precision, they usually have limitations including complex procedures, poor qualitative ability, and a lengthy testing period [5]. Those disadvantages have significantly resisted their utilization in large-scale rice quality inspection. Therefore, it is essential to develop a non-destructive and real-time measurement for linalool evaluation with excellent sensing properties.

There are various reports where researchers have employed commercially available gas sensors based on metal oxide semiconductors (e.g., tin oxide [6], zinc oxide [7], etc.) for the quantitative assessment of volatile

* Corresponding author.
E-mail: zhangc@yzu.edu.cn, zhangchao_cqu@hotmail.com

organic compounds (VOCs), including linalool. Among them, cerium oxide (CeO_2), being one of the most important rare earth semiconductors, has been thought as a promising material for VOC detection because its abundant crystal defects, high electrical conductivity, and good chemical stability [8,9]. Lyu *et al*. [10] constructed a hollow-structured CeO_2 for the detection of VOCs. And the sensor revealed a rapid response (6 s) and recovery time (11 s) towards 100 ppm acetone at 260 ℃. Nevertheless, the CeO_2 sensor operated at this optimal temperature, which was generally higher than the boiling point of VOCs, could result in the pyrolysis of the target gas. And this drawback hindered its further utilization in the inspection of rice quality. Therefore, to effectively identify the variations of linalool concentration in rice aging during storage, the operation of the as-developed sensor based on CeO_2 should be performed at low working temperatures, so that the linalool molecules will not decompose [11].

At low working temperatures, the sensors based on CeO_2 generally suffered from a low response and high limit of detection. To significantly improve the sensing properties of CeO_2 at low working temperatures, several strategic methods have been adopted. Liu *et al*. [12] synthesized mesoporous CeO_2 hollow tubules for the inspection of VOCs. And the sensing performance revealed that the response towards 100 ppm p-xylene was 12.4 at a relatively lower working temperature (133 ℃). The limit of detection of the optimal sensor was decreased to 100 ppb, which was the lowest value in the reported gas sensors based on CeO_2. Motaung *et al*. [13] constructed the heterojunction between CeO_2 and SnO_2 via a hydrothermal reaction. The sensor based on CeO_2–SnO_2 nano-composites exhibited an excellent response (~39.8) towards 20 ppm target gas at room temperature (RT). Unfortunately, CeO_2, as an ionic conductor, has inadequate adsorption sites, low conductivity, and high electrical resistance (1–10 GΩ) at RT, which dramatically influenced the linalool concentration that could be measured by the sensor. Additionally, most metal oxide semiconductor gas sensors have low sensitivity towards linalool macromolecules due to the chemical inertness of linalool, especially at RT.

Regulation of metal oxide semiconductors' electronic structure and surface chemical state is a feasible solution to develop the high-performance RT metal oxide semiconductor gas sensor. Oxygen vacancy engineering has been proved to be a promising pathway to optimize the crystal structure and surface activity of metal oxides, significantly improving the RT sensing performance [14,15]. Xu *et al*. [16] constructed a series of gas sensors based on SnO_2 thin films with different concentrations of oxygen vacancy via annealing under different temperatures in air for RT detection of VOCs. And the sensor revealed a high response of 150.5 towards 10 ppm trimethylamine. The excellent gas sensing performance could be ascribed for the formation of oxygen vacancy, which could dramatically enhance the carrier concentration in the conduction band and function as additional adsorption sites for the detection of VOCs. However, this method can only produce limited oxygen vacancy in metal oxide semiconductors only annealed under air atmosphere due to the lack of strong reducibility.

In this study, CeO_2 nanowires with various proportions of oxygen vacancy and Ce^{3+} ions were acquired via hydrothermal method combined with subsequent calcination under various controlled atmospheres (air, Ar, and 5%H_2+95%Ar). The morphology of nanowire provides more adsorption sites for redox reaction, and the valance states between Ce^{4+} and Ce^{3+} were regulated in the crystal, increasing or decreasing the contents of oxygen species. Moreover, this work focuses on the sensing properties, and reveals the sensor's RT sensing mechanism towards linalool. In the course of storage, with the changes of circumstances (e.g., period, temperature, humidity, etc.), the sensory quality of rice will deteriorate, displaying an unpleasant aroma profile. Consequently, the practicability of the as-developed gas sensor in rice quality inspection was verified by two varieties of rice (Indica and Japonica) stored at diverse periods (1, 3, 5, 7, 15, and 30 d). The results demonstrated that the work delivers a promising strategic material to develop high-performance RT electronic nose equipment to evaluate rice quality.

2 Experimental

2.1 Synthesis procedure

Oxygen vacancy engineering on CeO_2 nanowires was synthesized via hydrothermal method combined with subsequent calcination, as schematically illustrated in Fig. 1. Typically, 0.5 g $CeCl_3 \cdot 7H_2O$ was mixed with 20 mL of NaOH aqueous solution (10 M) after being continuously stirred at least 40 min. Then the above solutions were sealed in a 50 mL Teflon-lined stainless

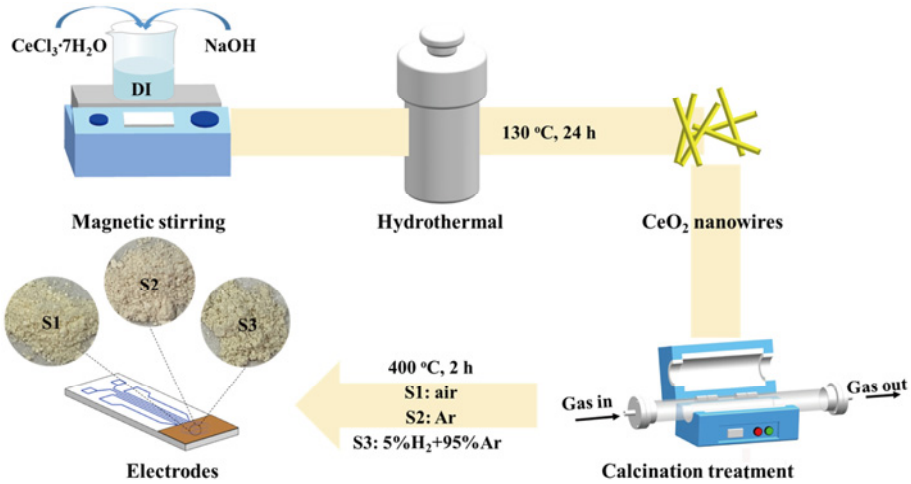

Fig. 1 Schematic illustrations of oxygen vacancy engineering on CeO_2 nanowires.

steel autoclave and maintained at 130 ℃ for 24 h. Naturally cooled down to RT, the solid precipitates were collected via centrifugation and rinsed alternately with deionized water (DI) and absolute ethanol to remove impurities, followed by drying in vacuum at 70 ℃ for 24 h. Ultimately, the precursors were annealed at 400 ℃ for 2 h with a heating rate of 3 ℃/min under different controlled atmospheres (air, Ar, and 5%H_2+95%Ar). Correspondingly, the as-obtained samples were designated as S1 (air), S2 (Ar), and S3 (5%H_2+95%Ar).

2. 2 Characterization

The morphologies and crystal structures of the as-obtained precipitates were inspected via the field emission-scanning electron microscope (FE-SEM; S4800, Hitachi, Japan) and transmission electron microscope (TEM; Tecnai 12, Philips, the Netherlands), and the X-ray diffractometer (D8 Advance, Bruker, Germany), respectively. The existence and surface chemical states of relevant elements were inspected via the high-angle annular dark-scanning transmission electron microscope (HAADF-STEM; Tecnai 12, Philips, the Netherlands) combined with the energy dispersive spectroscope (EDS; Tecnai 12, Philips, the Netherlands) and X-ray photoelectron spectroscope (XPS; ESCALAB250Xi, Thermo Fisher Scientific, USA). The specific surface areas of all the samples were investigated via nitrogen adsorption–desorption measurement based on Brunauer–Emmett–Teller (BET; Autosorb IQ3, Quantachrome Instruments, USA) method.

2. 3 Fabrication and measurement of sensors

All sensors were fabricated via mixing the powders with DI and grinding to be a homogeneous paste. Subsequently, the slurry was dip-coated onto the electrode. The experimental equipment employed in this experiment was based on Ref. [11]. Purified air (21%O_2+79%N_2) was bubbled through the liquid linalool. Then the resulting gas molecules were further diluted prior to being exposed to the sensitive materials. Additionally, the concentration of linalool gas was calculated by Eq. (1) [17] and controlled via mass flow controllers (MFCs; FS-200CV, Bronkhorst, Germany).

$$\text{Concentration}_{\text{linalool}}(\text{ppm}) = \frac{10^6 \times \text{Vapor pressure}_{\text{linalool}}}{760} \quad (1)$$

where $\text{Vapor pressure}_{\text{linalool}}$ represents the vapor pressure of liquid linalool, 0.17 mmHg at 25 ℃.

The sensing performance of the fabricated sensors was performed via a home-made gas tester (HCRK-SD101, Huachuang Ruike, China) under laboratory conditions (25±1 ℃, 30%±5% relative humidity (RH)). And the response was defined as the ratio between R_a and R_g, where R_a and R_g were the electrical resistances when the sensor was exposed to air and air/linalool mixture after reaching a steady state. The response (τ_{res}) and recovery (τ_{rec}) time was calculated as the time required for achieving 90% of the electrical resistance change during the adsorption and desorption of linalool.

3 Results and discussion

3. 1 Characterization of CeO_2 nanowires

To observe the morphologies and crystal structures of

all the precursors annealed under different controlled conditions, the FE-SEM images and diameter distributions of S1, S2, and S3 are displayed in Figs. 2(a)–2(c). It is apparent that all the powders exhibited nanowire morphology with an average diameter of 50±10 nm. This unique nanostructure has a high length–diameter ratio, large contact area, and modified physical and chemical properties, resulting in a large surface-to-volume ratio [18,19]. Except for nanowires' aggregation and partial fracture, the morphologies were not dramatically changed. And this fracture was chiefly because of the intense ultrasonic and agitation prior to the FE-SEM examination. To investigate the crystal structure of CeO_2 nanowires, the TEM image of S1 is revealed in Fig. 2(d). Both the FE-SEM and TEM images displayed the uniform diameter distribution of CeO_2 nanowires. As illustrated in Fig. 2(e), the spacing of lattice fringe, perpendicular to the growth direction, is 0.19 and 0.31 nm, corresponding to the (220) and (111) planes, respectively. Figure 2(f) depicts the selected area electron diffraction (SAED) image, indicating that the preferential growth direction was [110] [20]. Meanwhile, the HAADF-STEM image of S1 is demonstrated in Fig. 2(g). And the corresponding element mappings (Figs. 2(h) and 2(i)) display that the cerium (Ce) and oxygen (O) elements were uniformly distributed and co-existed. Hence, the CeO_2 nanowires were successfully synthesized and maintained through hydrothermal method combined with subsequent calcination under diverse conditions. Furthermore, the formation mechanism of the cubic CeO_2 nanowires is schematically demonstrated in Fig. 2(j). At high NaOH concentration (10 M), NaOH rapidly hydrolyzed to generate extensive OH^- in hydrothermal method, resulting in fast thermal hydrolysis of cerium ions at 130 ℃. Meanwhile, the high NaOH concentration might have a great influence on the stereo configuration of cerium complex similar to the cubic structure [21].

To investigate the crystal structures of CeO_2 nanowires annealed under different controlled conditions, the X-ray diffraction (XRD) analysis is depicted in Fig. 3(a). All the samples were monocrystalline, which was

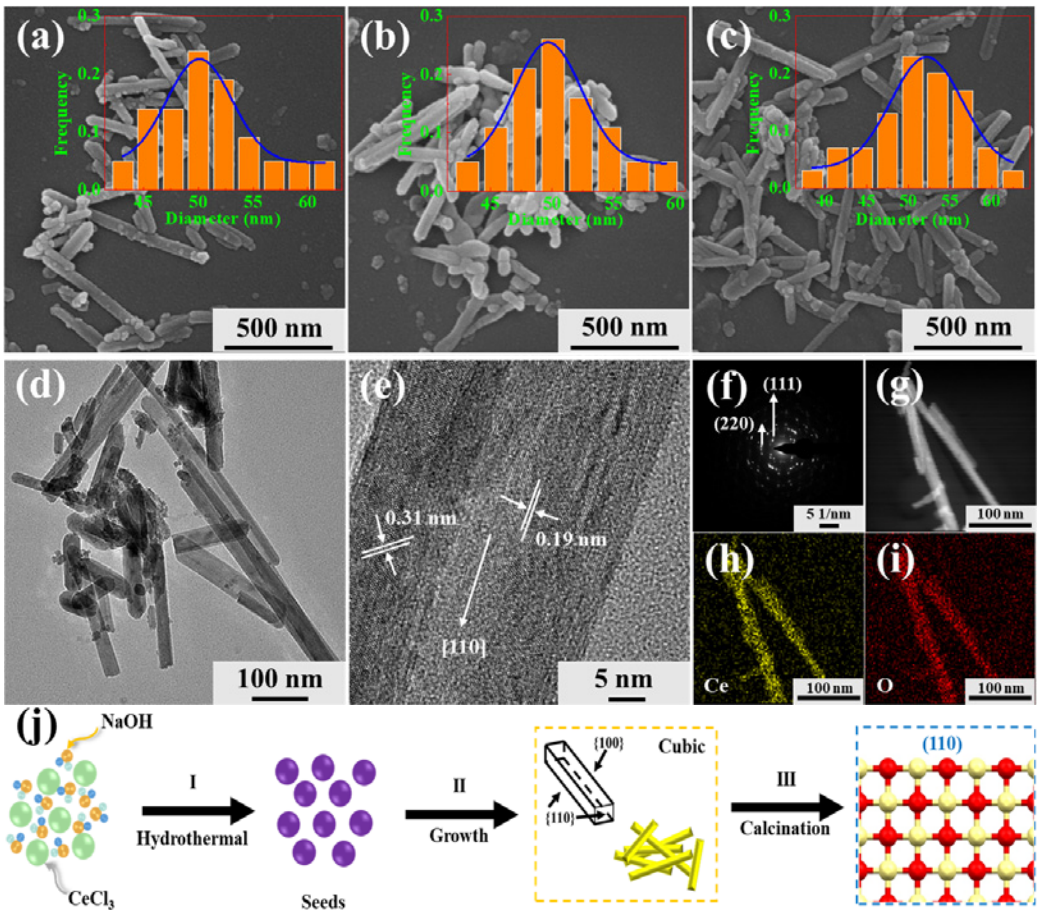

Fig. 2 (a–c) FE-SEM images of S1, S2, and S3; (d) TEM and (e) HRTEM images; (f) SAED image; (g) HAADF-STEM image; and (h, i) EDS mappings of S1. (j) Schematic diagram of formation mechanism of CeO_2 nanowires.

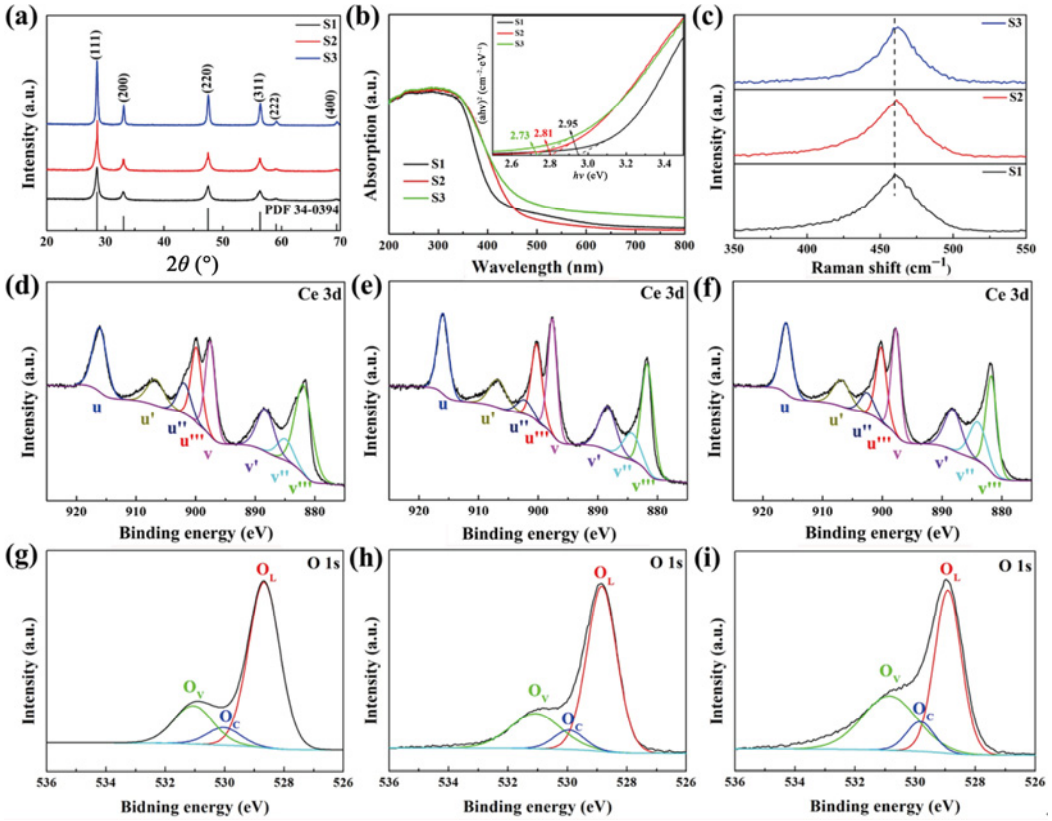

Fig. 3 (a) XRD patterns; (b) UV–Vis absorption spectra (the inset shows the corresponding Tauc spectra); (c) Raman spectra of S1, S2, and S3; and XPS analysis of Ce 3d and O 1s spectra for (d, g) S1, (e, h) S2, and (f, i) S3.

consistent with the TEM analysis, and the diffraction peaks were perfectly indexed to the fluorite-type CeO_2, corresponding to the face-centered cubic phases (PDF 34-0394). Besides, a prominent shift was not observed in the spectra, suggesting that the crystalline phase was maintained. Compared with the sample annealed under air, the peaks of S2 and S3 become sharper and stronger, which implies a higher crystallinity. The ultraviolet–visible (UV–Vis) absorption spectra of all the samples illustrated in Fig. 3(b) were analyzed to acquire the detailed information concerning the intrinsic performance. The spectra revealed that a large absorption tail was identified in the visible and near-infrared regions, which might be connected with the free electron and/or oxygen vacancy-induced polarons, indicating the existence of a larger number of oxygen vacancies [11,22]. As demonstrated in the inset in Fig. 3(b), the band gaps of the three samples calculated via Tauc equation were 2.95, 2.81, and 2.73 eV. The introduction of oxygen vacancy dramatically reduced the band gap, which was primarily because of the reduction from Ce^{4+} to Ce^{3+}, leading to the high conductivity of oxygen ions [23]. Raman spectra displayed in Fig. 3(c) indicated that the band of CeO_2 nanowires located at around 460 cm^{-1} could be generally ascribed for the Raman active vibrational mode of the fluorite-type structure. And compared with S1, the peaks of S2 and S3 slightly shifted towards a higher wavenumber, suggesting different oxygen vacancy contents because of the presence of lower oxidation state Ce^{3+} [24]. To effectively confirm the chemical compositions and oxidation states, the XPS analysis was also conducted. Figures 3(d)–3(f) reveal the Ce 3d spectra of all the as-synthesized samples. These spectra were deconvolved into eight peaks, corresponding to two kinds of oxidation states of Ce ions. The peaks (u" and v") were attributed to Ce^{3+} oxidation states, whereas the peaks (u, u', u"', v, v', and v"') were ascribed for Ce^{4+} [25,26]. Ce^{3+} oxidation states implied the existence of unsaturated chemical bonds and oxygen vacancy. According to Ref. [27], the integrated areas of Ce^{4+} and Ce^{3+} were calculated, as summarized in Table 1. And then, the concentrations of Ce^{3+} in S1, S2, and S3 were estimated to be around 0.12, 0.17, and 0.19, respectively (Table 2). It is obvious that S3 exhibited a higher concentration of Ce^{3+} ions, which might be closely related to the positively-

Table 1 Integrated areas of individual XPS peaks of Ce 3d in S1, S2, and S3

	Ce $3d_{3/2}$				Ce $3d_{5/2}$			
	u	u'	u''	u'''	v	v'	v''	v'''
S1	118,785	56,892	50,114	92,002	101,392	192,503	43,524	115,440
S2	58,886	37,291	14,298	36,116	63,649	102,068	68,182	83,519
S3	97,436	66,359	38,520	104,897	119,308	158,139	123,977	142,368

Table 2 Concentrations of Ce^{3+} and Ce^{4+} ions and stoichiometry ratios of CeO_2 nanowires annealed under different controlled conditions

	Concentration					Stoichiometry ratio	
	Ce^{3+}	Ce^{4+}	O_L	O_C	O_V	x^a	x'^b
S1	0.12	0.88	0.72	0.11	0.17	1.94	1.75
S2	0.17	0.83	0.59	0.13	0.28	1.92	1.56
S3	0.19	0.81	0.51	0.16	0.33	1.91	1.27

Note: $^a x = [O]/[Ce] = 1.5Ce^{3+} + 2Ce^{4+}$, $^b x' = [O_{1s}]/[Ce_{3d}] = (A_O/A_{Ce}) \times (S_{Ce}/S_O)$, where $S_{Ce} = 7.399$, and $S_O = 0.711$.

charged Ce ions with accompanying charge compensated electrons [28]. The generation of defective structures has been closely related to the interaction between metal oxides and hydrogen via losing the lattice oxygen (O_L) bonded with Ce–O–Ce to form oxygen vacancy (O_V) based on the following process (Reaction (2)) [29]. Accordingly, regulating the electronic structure and surface chemical states of CeO_2 nanowires with different oxygen vacancy contents via a simple method, including annealing the precursor under different controlled atmospheres, made them become the promising strategic materials for sensing application. Additionally, the O 1s spectra demonstrated in Figs. 3(g)–3(i) can be divided well to three Gaussian–Lorenz peaks centered at around 528.6, 529.8, and 530.9 eV, accounting for O_L, surface chemisorbed oxygen (O_C), and O_V, respectively [30]. And the relative quantitative analysis of O 1s spectra is also illustrated in Table 2. The value of x' ($x' = [O_{1s}]/[Ce_{3d}]$) was smaller than that of x ($x = [O]/[Ce]$), confirming that the formation of oxygen vacancy was accompanied by an increase of Ce^{3+} ion. The existence of oxygen vacancy will generate adequate adsorption sites, improving the proportion of absorbed oxygen species participated in the redox reaction [14]. Additionally, as illustrated in Fig. 4, the specific surface areas of S1, S2, and S3 were 14.54, 32.91, and 83.95 m^2/g, respectively, indicating that the surface chemical states were modified after annealing under different controlled conditions. Consequently, the sample with high specific surface area was beneficial to adsorbing target gas molecules, contributing to significantly enhancing the gas sensing performance of S3.

$$3Ce^{4+} + O_L + H_2(g) \rightarrow 4Ce^{3+} + O_V + H_2O \quad (2)$$

3.2 Gas sensing performance

RT gas sensing performance of S1, S2, and S3 was comprehensively investigated. Figure 5(a) shows the variations of electrical resistance of the sensors towards various concentrations of linalool. The resistance increased when exposed to purified air and eventually displayed a high state ranging from 1 to 10 GΩ. Once linalool was introduced into the testing chamber, the resistance decreased. When the purified air was released again, the resistance returned to R_a, indicating that all sensors exhibited n-type characteristics. Besides, it can be seen that the R_a of S2 and S3 decreased, which could be ascribed for the influence of oxygen vacancy. Normally, electrons trapped in the donor level were directly excited into the conduction band of the sample, increasing the carrier concentration of conduction band, and eventually displaying lower electrical resistance (R_a) [31,32]. As seen from Fig. 5(b), it is obvious that controlling the annealing atmosphere significantly influences the gas response, and all the sensors demonstrated an excellent positive linear correlation with the ppm-level linalool concentration. The S3

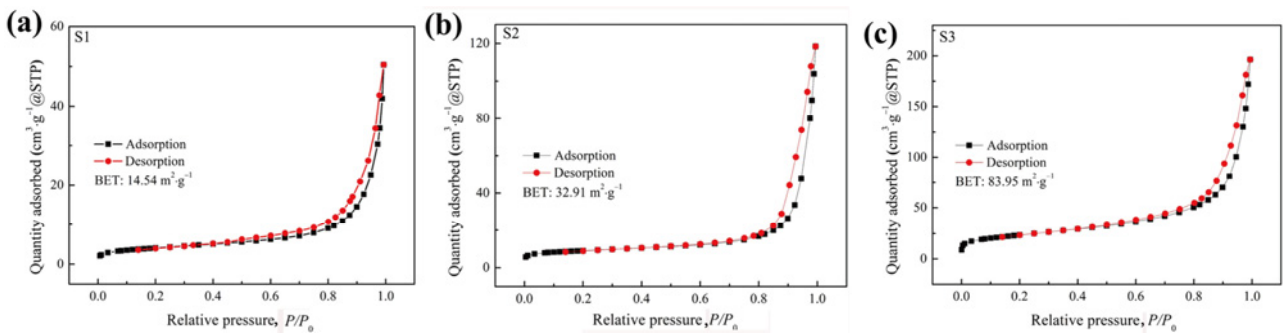

Fig. 4 N_2 adsorption and desorption isotherms of S1, S2, and S3.

revealed the highest response towards linalool. Specifically, the gas response of S3 towards 20 ppm linalool is 16.7, which is approximately 3.2 and 2.4 times higher than those of S1 and S2 (Fig. 5(c)), respectively. This enhancement was nearly similar to the sequence of increasing O_V concentration measured by the XPS (Table 2), which was chiefly due to that the presence of oxygen vacancies efficiently increased the concentration of adsorbed oxygen, thus contributing to an increase in response. Besides, the specific surface area of S3 illustrated in Fig. 4 was 83.95 m^2/g, which was much larger than those of S1 (14.54 m^2/g) and S2 (32.91 m^2/g). And a higher specific surface area could provide adequate sites for the adsorption of linalool molecules, thus contributing to a higher sensor response. Meanwhile, it is worth noting that S3 was not inclined to be saturated even if the concentration of linalool achieved 20 ppm, displaying that the as-developed sensor could be able to inspect linalool at a wide range. Hence, it turns out that S3 shows excellent RT gas sensing performance and is also available for a wide range of linalool sensing. And based on Ref. [33], the detection limit for linalool in S3 was calculated to be approximately 0.54 ppm. The dynamic response–recovery curves towards 20 ppm linalool shown in Fig. 5(d) are also analyzed to assess the sensing properties of the sensor. It can be calculated that the τ_{res} and τ_{rec} were 26 and 144 s (S1), 21 and 131 s (S2), and 16 and 121 s (S3), respectively. The short response time might be due to the rapid diffusion of linalool among the CeO_2 sensitive layers. While the τ_{rec} was long, primarily because the energy obtained from RT was much lower than the activation energy for linalool molecule desorption [34]. In view of practical application of the as-developed sensor, an outstanding capability is to distinguish linalool from various atmospheres [35]. We also investigated the selectivity of all the sensors towards 20 ppm of different kinds of target gases (NH_3, NO_2, CO_2, $C_9H_{18}O$, and C_5H_5N), as illustrated in Fig. 5(e). These results indicate that S3 has superior selectivity to linalool gas. This might be primarily accounted that the ethyl groups in linalool led to the

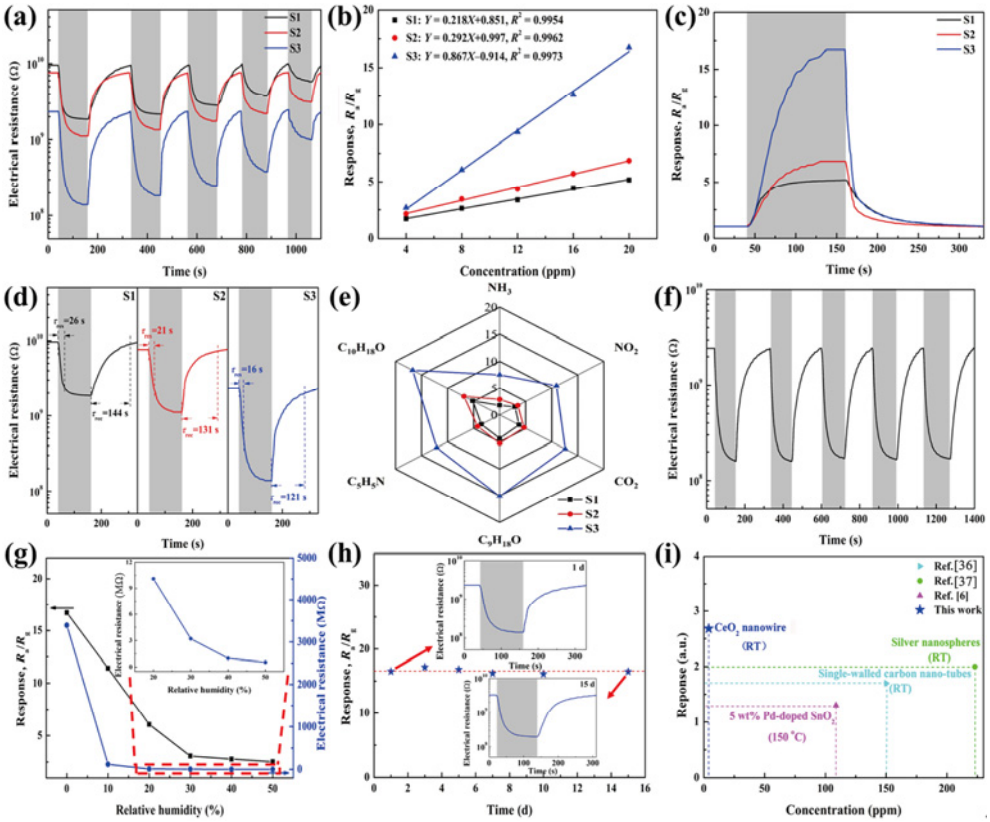

Fig. 5 (a) Changes in electrical resistance towards different concentrations of ppm-level linalool at RT; (b) linear relationship between response and concentrations (4–20 ppm); (c) responses and (d) dynamic response–recovery curves of S1, S2, and S3 to 20 ppm linalool; (e) responses of S1, S2, and S3 to 20 ppm different target gases; (f) reproducibility of S3 to 20 ppm linalool; (g) response and electrical resistance of S3 to 20 ppm linalool under various RH; (h) long-term stability of S3 to 20 ppm linalool; and (i) gas-sensing performance in comparison with other state-of-the-art linalool sensors.

highest electron-donating ability among various atmospheres [16]. Besides, more oxygen vacancies in S3 could promote the adsorption of linalool molecules, which was due to the strong electron affinity interaction between linalool molecules with oxygen vacancy [38]. Consequently, linalool molecules were more easily adsorbed onto the CeO_2 sensitive layer and reacted with its chemisorbed oxygen to reach a higher response. Moreover, the responses to 20 ppm linalool were measured within five cycles to verify the repeatability of S3 (Fig. 5(f)), and there are no major changes in R_a and gas response, indicating excellent repeatability. Additionally, it is well recognized that humidity will exert a substantial influence upon the application of sensor. Therefore, the responses and R_a towards 20 ppm linalool under various RH were calculated to investigate the effect of RH on S3. With the RH ranging from 0% to 30%, the response significantly decreased from 16.7 to 3.1. This is owing to the introduction of water, decreasing the number of active sites and impeding the adsorption of linalool molecules [39]. Meanwhile, the chemisorbed oxygen species reacted with H_2O molecules decreased the R_a (the inset in Fig. 5(g)) and the sensor response [40]. Moreover, long-term stability was also a crucial factor for further evaluating the service life of sensor. As shown in Fig. 5(h), there is no obvious attenuation and fluctuation on both response and R_a towards 20 ppm linalool within 15 d, demonstrating good long-term stability. Additionally, the gas-sensing performance compared with other state-of-the-art linalool sensors operated at a low temperature (150 ℃) or RT (Fig. 5(i)) indicated that S3 with extensive oxygen vacancies still displayed a good sensor response even at a lower concentration of linalool. Hence, it is a competitive linalool sensor, which could be employed to inspect rice aging.

3. 3 Gas sensing mechanism

According to the characteristic space charge model of n-type metal oxide semiconductors, the RT gas sensing mechanism of S3 towards ppm-level linalool was proposed, as illustrated in Fig. 6. Specifically, when exposed to purified air, oxygen molecules were adsorbed onto CeO_2 sensing materials and captured free electron from the conduction band to generate the adsorbed oxygen species (O_2^-) [41], simultaneously producing an electron depletion region and a potential barrier (Figs. 6(a) and 6(c)), contributing to a decrease in the electron concentration of CeO_2, and displaying an increase in the resistance [42,43]. While linalool gas was introduced, $C_{10}H_{18}O(g)$ was firstly transformed into $C_{10}H_{18}O(ad)$ (Reaction (3)) [11]. And then the redox reaction between $C_{10}H_{18}O(ad)$ and O_2^- was performed.

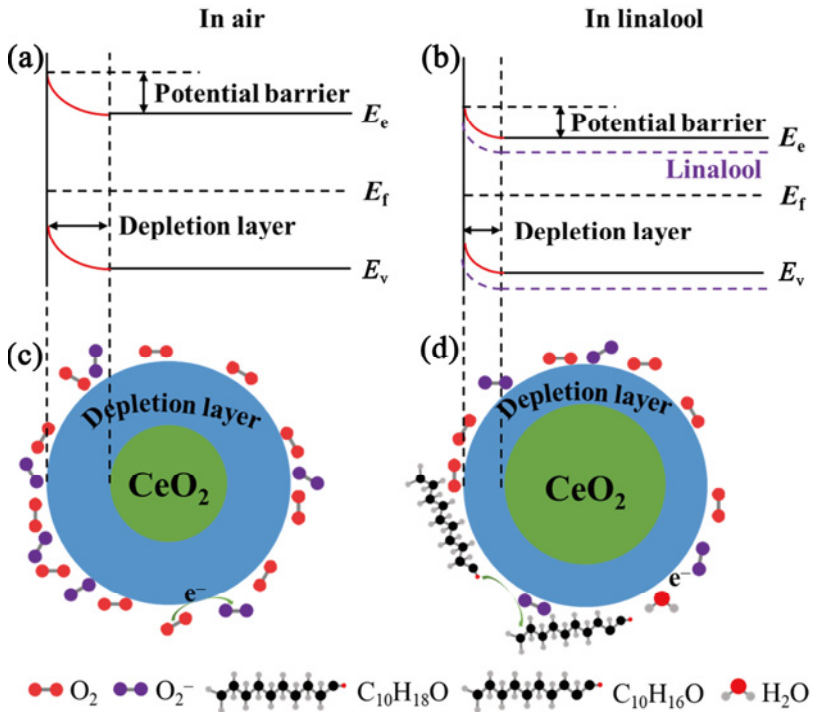

Fig. 6 Schematic illustration of RT sensing mechanism of S3 towards ppm-level linalool: (a, c) in air; (b, d) in linalool (E_c: conduction band bottom; E_f: Fermi level; E_v: valence band top).

The ultimate reaction could generate $C_{10}H_{16}O$(ad), H_2O(g), and free electrons (Reaction (4)), decreasing the depletion region and potential barrier (Figs. 6(b) and 6(d)) [44]. Owing to the release of electrons onto the conduction band of the sensing material, the sensor subsequently showed a decrease in electrical resistance [45,46].

$$C_{10}H_{18}O(g) \rightarrow C_{10}H_{18}O(ad) \quad (3)$$

$$2C_{10}H_{18}O(ad) + O_2^-(ad) \rightarrow 2C_{10}H_{16}O(ad) + 2H_2O(g) + e^- \quad (4)$$

The enhanced RT sensing performance of S3 for linalool is generally owing to the following aspects: the nanowire morphology, high specific surface area, and increased percentage of O_V and O_C. The nanowire structure with a large surface-to-volume ratio could offer a feasible pathway for the transmission and diffusion of linalool. Secondly, the S3 manifested a larger specific surface area of 83.95 m^2/g, which was beneficial to the adsorption of linalool gas, resulting in an excellent sensor response [47,48]. Thirdly, the percentage of O_V and O_C in S3 measured from the XPS analysis (Table 2) was larger than that of S1 and S2, providing adequate adsorption sites for the redox reaction. Additionally, Ce^{3+} would replace Ce^{4+}, and oxygen vacancy would also produce to reach the balance of charge [49,50]. Hence, the proportion of O_V was further increased, and the negative charge was released onto the conduction band, simultaneously increasing the carrier concentration [51–53].

3. 4 Practicability of gas sensor

To effectively verify the practicability of the as-developed sensor in rice quality inspection during storage, the variations of electrical resistance of the sensor based on S3 exposed to the resulting VOCs, generated from two kinds of rice (Indica and Japonica rice) stored in various periods (1, 3, 5, 7, 15, and 30 d), were monitored (Fig. 7(a)). As shown in Fig. 7(b), the response towards the VOCs produced via aging of Indica rice was 80.2, which was around 2.2 times higher than that of Japonica rice (36.1), demonstrating that the S3 may be able to distinguish Indica rice from Japonica rice. Additionally, in Fig. 7(c), the response fluctuated slightly within different storage periods (3, 5, 7, 15, and 30 d). This was chiefly because of the slow aging process of Indica rice [1,5,11], and the testing conditions, including temperature, air pressure, and humidity would also have a substantial influence upon the response obtained from this study. The experimental results illustrate that the sensor based on S3 may have a tremendous application prospect in inspecting rice quality during storage.

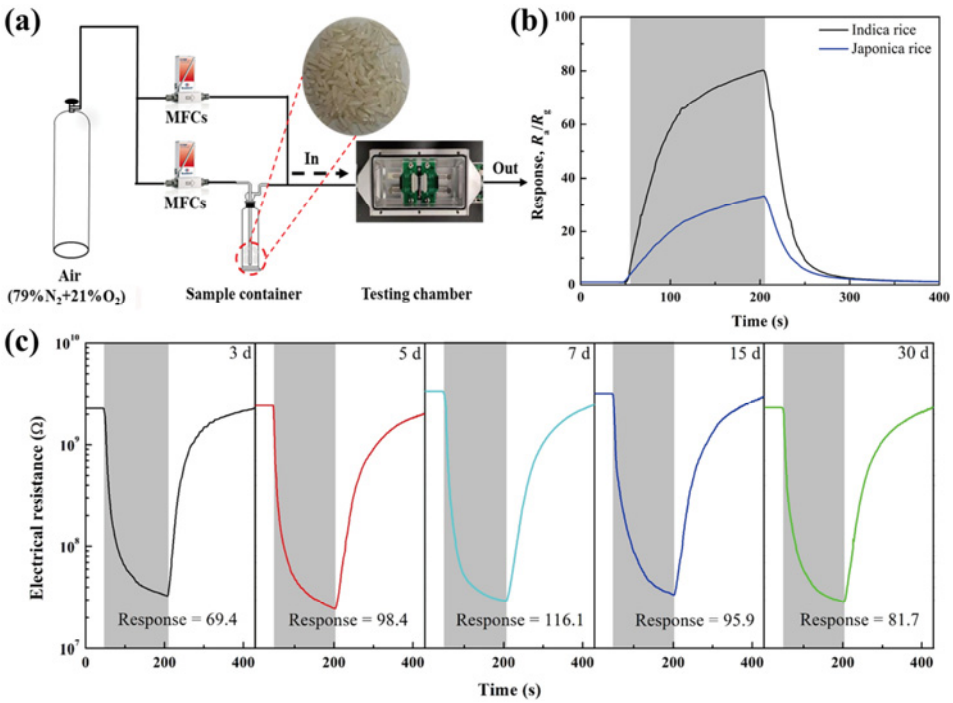

Fig. 7 (a) Schematic diagram of the sensor testing system for detecting VOCs generated from 30 g Indica and Japonica rice; (b) response measured under exposure to VOCs generated from two rice aging; and (c) response towards VOCs generated from 30 g Indica rice stored in various periods.

4 Conclusions

In this study, oxygen vacancy engineering on CeO_2 nanowires was developed through simple hydrothermal method combined with calcination under different controlled atmospheres (air, Ar, and 5%H_2+95%Ar). The results revealed that the S3 exhibited outstanding sensing properties towards ppm-level linalool at RT. This enhanced sensing performance can be ascribed for (1) the nanowire morphology with a high surface-to-volume ratio was advantageous to the transmission and diffusion of linalool; (2) S3 exhibited a larger specific surface area (83.95 m^2/g), providing adequate adsorption sites for the adsorption of linalool; (3) an increase in O_V and O_C components was accompanied by an increase of Ce^{3+} ions through annealing under 5%H_2+95%Ar atmosphere, increasing the oxygen species that reacted with linalool. Additionally, the practical experiment also manifested that the S3 sensor was able to distinguish Indica rice from Japonica rice and monitor rice quality changes during storage. Hence, this study anticipates providing a tremendous application prospect in the research and development of high-performance RT electronic nose equipment utilization for a large-scale inspection of rice quality during aging.

Acknowledgements

This work was supported by the National Natural Science Foundation of China (No. 51872254), the Outstanding Youth Foundation of Jiangsu Province of China (No. BK20211548), and the Excellent Doctoral Dissertation Fund of Yangzhou University (2022).

Declaration of competing interest

The authors have no competing interests to declare that are relevant to the content of this article.

References

[1] Hu XQ, Lu L, Guo ZL, *et al*. Volatile compounds, affecting factors and evaluation methods for rice aroma: A review. *Trends Food Sci Technol* 2020, **97**: 136–146.

[2] Arbid Y, Sleiman M, Richard C. Photochemical interactions between pesticides and plant volatiles. *Sci Total Environ* 2022, **807**: 150716.

[3] Qin HW, Yang SB, Yang MQ, *et al*. Effects on volatile oil and volatile compounds of *Amomum tsao-ko* with different pre-drying and drying methods. *Ind Crop Prod* 2021, **174**: 114168.

[4] Shi J, Nian YQ, Da DD, *et al*. Characterization of flavor volatile compounds in sauce spareribs by gas chromatography–mass spectrometry and electronic nose. *LWT* 2020, **124**: 109182.

[5] Xu JY, Liu KW, Zhang C. Electronic nose for volatile organic compounds analysis in rice aging. *Trends Food Sci Technol* 2021, **109**: 83–93.

[6] Kakoty P, Bhuyan M, Das K. Performance of Pd doped SnO_2 as sensing material for tea aromatic chemicals. *IEEE Sens J* 2018, **18**: 4392–4398.

[7] Jan FA, Wajidullah, Ullah R, *et al*. Exploring the environmental and potential therapeutic applications of *Myrtus communis L*. assisted synthesized zinc oxide (ZnO) and iron doped zinc oxide (Fe–ZnO) nanoparticles. *J Saudi Chem Soc* 2021, **25**: 101278.

[8] Liu JS, Zhen YX, Zhang XF, *et al*. Bio-template synthesis of CeO_2 ultrathin nanosheets for highly selective and sensitive detection of ppb-level p-xylene vapor. *Ceram Int* 2022, **48**: 1550–1559.

[9] Yang WT, Wang X, Song SY, *et al*. Syntheses and applications of noble-metal-free CeO_2-based mixed-oxide nanocatalysts. *Chem* 2019, **5**: 1743–1774.

[10] Lyu L, Xie Q, Yang YY, *et al*. A novel CeO_2 hollow–shell sensor constructed for high sensitivity of acetone gas detection. *Appl Surf Sci* 2022, **571**: 151337.

[11] Zhang C, Xu JY, Li HP, *et al*. Role of ruthenium incorporation on room-temperature nonanal sensing properties of Ru-loaded urchin-like $W_{18}O_{49}$ hierarchical nanostructure. *Sensor Actuat B Chem* 2022, **353**: 131096.

[12] Liu JS, Song BY, Huang J, *et al*. Absorbent cotton derived mesoporous CeO_2 hollow tubule for enhanced detection of p-xylene at low energy consumption. *J Alloys Compd* 2021, **873**: 159774.

[13] Motaung DE, Tshabalala ZP, Makgwane PR, *et al*. Multi-functioning of CeO_2–SnO_2 heterostructure as room temperature ferromagnetism and chemiresistive sensors. *J Alloys Compd* 2022, **906**: 164317.

[14] Yuan H, Aljneibi SAAA, Yuan J, *et al*. ZnO nanosheets abundant in oxygen vacancies derived from metal–organic frameworks for ppb-level gas sensing. *Adv Mater* 2019, **31**: 1807161.

[15] Huan YC, Wu KD, Li CJ, *et al*. Micro-nano structured functional coatings deposited by liquid plasma spraying. *J Adv Ceram* 2020, **9**: 517–534.

[16] Xu YS, Zheng LL, Yang C, *et al*. Oxygen vacancies enabled porous SnO_2 thin films for highly sensitive detection of triethylamine at room temperature. *ACS Appl Mater Interfaces* 2020, **12**: 20704–20713.

[17] Liu G, Froudarakis E, Patel JM, *et al*. Target specific functions of EPL interneurons in olfactory circuits. *Nat Commun* 2019, **10**: 3369.

[18] Meng JP, Li Z. Schottky-contacted nanowire sensors. *Adv Mater* 2020, **32**: 2000130.

[19] Liu H, Zhang HY, Zhu WH, *et al*. Crystalline-to-amorphous phase transformation in CuO nanowires for gaseous ionization and sensing application. *ACS Sensors* 2021, **6**: 4118–4125.

[20] Li GN, Wang B, Resasco DE. Water promotion (or inhibition) of condensation reactions depends on exposed cerium oxide catalyst facets. *ACS Catal* 2020, **10**: 5373–5382.

[21] Cao S, Sui N, Zhang P, *et al*. TiO_2 nanostructures with different crystal phases for sensitive acetone gas sensors. *J Colloid Interface Sci* 2022, **607**: 357–366.

[22] Chen HY, Song LZ, Ouyang SX, *et al*. Co and Fe codoped $WO_{2.72}$ as alkaline-solution-available oxygen evolution reaction catalyst to construct photovoltaic water splitting system with solar-to-hydrogen efficiency of 16.9%. *Adv Sci* 2019, **6**: 1900465.

[23] Wondimu TH, Chen GC, Chen HY, *et al*. High catalytic activity of oxygen-vacancy-rich tungsten oxide nanowires supported by nitrogen-doped reduced graphene oxide for the hydrogen evolution reaction. *J Mater Chem A* 2018, **6**: 19767–19774.

[24] Gao W, Zhang ZY, Li J, *et al*. Surface engineering on CeO_2 nanorods by chemical redox etching and their enhanced catalytic activity for CO oxidation. *Nanoscale* 2015, **7**: 11686–11691.

[25] Sun HM, Tian CY, Fan GL, *et al*. Boosting activity on Co_4N porous nanosheet by coupling CeO_2 for efficient electrochemical overall water splitting at high current densities. *Adv Funct Mater* 2020, **30**: 1910596.

[26] Hassandoost R, Pouran SR, Khataee A, *et al*. Hierarchically structured ternary heterojunctions based on Ce^{3+}/Ce^{4+} modified Fe_3O_4 nanoparticles anchored onto graphene oxide sheets as magnetic visible-light-active photocatalysts for decontamination of oxytetracycline. *J Hazard Mater* 2019, **376**: 200–211.

[27] Putla S, Amin MH, Reddy BM, *et al*. MnO_x nanoparticle-dispersed CeO_2 nanocubes: A remarkable heteronanostructured system with unusual structural characteristics and superior catalytic performance. *ACS Appl Mater Interfaces* 2015, **7**: 16525–16535.

[28] Cong S, Yuan YY, Chen ZG, *et al*. Noble metal-comparable SERS enhancement from semiconducting metal oxides by making oxygen vacancies. *Nat Commun* 2015, **6**: 7800.

[29] Bayeh AW, Lin GY, Chang YC, *et al*. Oxygen-vacancy-rich cubic CeO_2 nanowires as catalysts for vanadium redox flow batteries. *ACS Sustain Chem Eng* 2020, **8**: 16757–16765.

[30] Bi H, Zhang LX, Xing Y, *et al*. Morphology-controlled synthesis of CeO_2 nanocrystals and their facet-dependent gas sensing properties. *Sensor Actuat B Chem* 2021, **330**: 129374.

[31] Zhao YX, Chang C, Teng F, *et al*. Defect-engineered ultrathin δ-MnO_2 nanosheet arrays as bifunctional electrodes for efficient overall water splitting. *Adv Energy Mater* 2017, **7**: 1700005.

[32] Luo N, Wang C, Zhang D, *et al*. Ultralow detection limit MEMS hydrogen sensor based on SnO_2 with oxygen vacancies. *Sensor Actuat B Chem* 2022, **354**: 130982.

[33] Zhang C, Li Y, Liu GF, *et al*. Room temperature NO_2 sensing properties of $ZnO_{1-\alpha}$ coating prepared by hydrogen reduction method. *Ceram Int* 2021, **47**: 29873–29880.

[34] Ju DX, Xu HY, Qiu ZW, *et al*. Near room temperature, fast-response, and highly sensitive triethylamine sensor assembled with Au-loaded ZnO/SnO_2 core–shell nanorods on flat alumina substrates. *ACS Appl Mater Interfaces* 2015, **7**: 19163–19171.

[35] Huang CZ, Adimi S, Liu DL, *et al*. Mesoporous titanium niobium nitrides supported Pt nanoparticles for highly selective and sensitive formaldehyde sensing. *J Mater Chem A* 2021, **9**: 19840–19846.

[36] Wang H, Ramnani P, Pham T, *et al*. Gas biosensor arrays based on single-stranded DNA-functionalized single-walled carbon nanotubes for the detection of volatile organic compound biomarkers released by Huanglongbing disease-infected citrus trees. *Sensors* 2019, **19**: 4795.

[37] Shahar T, Feldheim G, Marx S, *et al*. Core–shell nanoparticles for gas phase detection based on silver nanospheres coated with a thin molecularly imprinted polymer adsorbed on a chemiresistor. *Nanoscale* 2018, **10**: 17593–17602.

[38] Wang TS, Liu SY, Sun P, *et al*. Unexpected and enhanced electrostatic adsorption capacity of oxygen vacancy-rich cobalt-doped In_2O_3 for high-sensitive MEMS toluene sensor. *Sensor Actuat B Chem* 2021, **342**: 129949.

[39] Qu FD, Zhang SD, Huang CZ, *et al*. Surface functionalized sensors for humidity-independent gas detection. *Angew Chem Int Ed* 2021, **60**: 6561–6566.

[40] Bai HN, Guo H, Wang J, *et al*. Hydrogen gas sensor based on SnO_2 nanospheres modified with Sb_2O_3 prepared by one-step solvothermal route. *Sensor Actuat B Chem* 2021, **331**: 129441.

[41] Liang HP, Guo LP, Cao NJ, *et al*. Practical room temperature formaldehyde sensing based on a combination of visible-light activation and dipole modification. *J Mater Chem A* 2021, **9**: 23955–23967.

[42] Zhang C, Huan YC, Li Y, *et al*. Low concentration isopropanol gas sensing properties of Ag nanoparticles decorated In_2O_3 hollow spheres. *J Adv Ceram* 2022, **11**: 379–391.

[43] Ma JH, Ren Y, Zhou XR, *et al*. Pt nanoparticles sensitized ordered mesoporous WO_3 semiconductor: Gas sensing performance and mechanism study. *Adv Funct Mater* 2018, **28**: 1705268.

[44] Zhang C, Li Y, Liu GF, *et al*. Preparation of ZnO_{1-x} by peroxide thermal decomposition and its room temperature gas sensing properties. *Rare Metals* 2022, **41**: 871–876.

[45] Wang J, Chen FM, Guo Q, *et al*. Light-addressable square wave voltammetry (LASWV) based on a field-effect structure for electrochemical sensing and imaging. *ACS Sensors* 2021, **6**: 1636–1642.

[46] Sadeghzadeh-Attar A. Photocatalytic degradation evaluation of N–Fe codoped aligned TiO_2 nanorods based on the effect

of annealing temperature. *J Adv Ceram* 2020, **9**: 107–122.
[47] Li J, Yang M, Cheng XL, *et al*. Fast detection of NO_2 by porous SnO_2 nanotoast sensor at low temperature. *J Hazard Mater* 2021, **419**: 126414.
[48] Liu D, Ren XW, Li YS, *et al*. Nanowires-assembled WO_3 nanomesh for fast detection of ppb-level NO_2 at low temperature. *J Adv Ceram* 2020, **9**: 17–26.
[49] Bui HT, Weon S, Bae JW, *et al*. Oxygen vacancy engineering of cerium oxide for the selective photocatalytic oxidation of aromatic pollutants. *J Hazard Mater* 2021, **404**: 123976.
[50] Lee J, Choi Y, Park BJ, *et al*. Precise control of surface oxygen vacancies in ZnO nanoparticles for extremely high acetone sensing response. *J Adv Ceram* 2022, **11**: 769–783.
[51] Li Y, Lu YL, Wu KD, *et al*. Microwave-assisted hydrothermal synthesis of copper oxide-based gas-sensitive nanostructures. *Rare Metals* 2021, **40**: 1477–1493.
[52] Yao MS, Li WH, Xu G. Metal–organic frameworks and their derivatives for electrically-transduced gas sensors. *Coordin Chem Rev* 2021, **426**: 213479.
[53] Zhang Y, Han S, Wang MY, *et al*. Electrospun Cu-doped In_2O_3 hollow nanofibers with enhanced H_2S gas sensing performance. *J Adv Ceram* 2022, **11**: 427–442.